ELSEVIER

Mechanistic and thermodynamic characterization of oxathiazolones as potent and selective covalent immunoproteasome inhibitors

Check for updates

Levente M. Mihalovits [*], György G. Ferenczy, György M. Keserű [*]

Medicinal Chemistry Research Group, Research Centre for Natural Sciences, Magyar tudósok körútja 2, Budapest 1117, Hungary

A R T I C L E   I N F O

A B S T R A C T

The ubiquitin–proteasome system is responsible for the degradation of proteins and plays a critical role in key cellular processes. While the constitutive proteasome (cPS) is expressed in all eukaryotic cells, the immunoproteasome (iPS) is primarily induced during disease processes, and its inhibition is beneficial in the treatment of cancer, autoimmune disorders and neurodegenerative diseases. Oxathiazolones were reported to selectively inhibit iPS over cPS, and the inhibitory activity of several oxathiazolones against iPS was experimentally determined. However, the detailed mechanism of the chemical reaction leading to irreversible iPS inhibition and the key selectivity drivers are unknown, and separate characterization of the noncovalent and covalent inhibition steps is not available for several compounds. Here, we investigate the chemical reaction between oxathiazolones and the Thr1 residue of iPS by quantum mechanics/ molecular mechanics (QM/MM) simulations to establish a plausible reaction mechanism and to determine the rate-determining step of covalent complex formation. The modelled binding mode and reaction mechanism are in line with the selective inhibition of iPS versus cPS by oxathiazolones. The k_{inact} value of several ligands was estimated by constructing the potential of mean force of the rate-determining step by QM/MM simulations coupled with umbrella sampling. The equilibrium constant K_i of the noncovalent complex formation was evaluated by classical force field-based thermodynamic integration. The calculated K_i and k_{inact} values made it possible to analyse the contribution of the noncovalent and covalent steps to the overall inhibitory activity. Compounds with similar intrinsic reactivities exhibit varying selectivities for iPS versus cPS owing to subtle differences in the binding modes that slightly affect K_i, the noncovalent affinity, and importantly alter k_{inact}, the covalent reactivity of the bound compounds. A detailed understanding of the inhibitory mechanism of oxathiazolones is useful in designing iPS selective inhibitors with improved drug-like properties.

1. Introduction

The proteasome plays a crucial role in nonlysosomal protein degradation [1] through the ubiquitin–proteasome system (UPS). The UPS is essential in a diverse set of cellular actions, such as maintaining cell homeostasis, removing misfolded proteins, controlling cell cycle progression and regulating the immune system. Owing to its importance in homeostasis, malfunctions of the UPS imply different pathogenic processes, such as neoplastic, autoimmune, autoinflammatory, and neurodegenerative disorders [2,3]. The recognition of UPS-based diseases has driven attention to the development of proteasome inhibitors. Notable examples of

FDA-approved proteasome inhibitors are bortezomib and carfilzomib, both of which are applied in the treatment of multiple myeloma [4,5].

The proteasome is an ATP-dependent N-terminal hydrolase found in eukaryotes and in prokaryotes [6]. It has a barrel shape and consists of 28 subunits, most notably enzymatically active subunits β1, β2 and β5 [7]. These three subunits are the key structural elements differentiating the constitutive proteasome (c-20s) from the immunoproteasome (i-20s), the latter of which is composed of subunits β1i, β2i and β5i. The immunoproteasome is part of the immune system and is expressed predominantly in conventional dendritic and plasmacytoid dendritic cells and in lymphocytes. Nonhaematopoietic cells can also express the immunoproteasome by cytokines such as IFN-γ or TNF-α [8-10]. All three catalytically active subunits mentioned above have an N-terminal threonine residue that is able to initiate a nucleophilic

* Corresponding author.
  E-mail addresses: mihalovits.levente@ttk.hu (L.M. Mihalovits), ferenczy.gyorgy@ttk.hu (G.G. Ferenczy), keseru.gyorgy@ttk.hu (G.M. Keserű).

attack on various ligands and is the primary target of covalent inhibitors of the proteasomes.

Noncovalent proteasome inhibitors include peptide-like compounds occupying the substrate binding channel and protruding into nonprimed and primed specificity pockets [5]. Nonpeptidic inhibitor binding to the specificity pocket has also been reported [11]. Covalent inhibitors typically bind to the Thr1 residue with warhead-dependent mechanisms. The most notable covalent inhibitor types are aldehydes, acrylamides, vinyl sulfones, boronates, α, β-epoxyketones, α-ketoaldehydes, β-lactones and oxazole derivatives [5,12]. Although higher toxicity and less selectivity of proteasome inhibitors are acceptable in the treatment of advanced malignancies, therapeutic usage in nonmalignant diseases requires elaborate inhibitor design methods. Previous examinations showed that inhibitors with immunoproteasome (iPS) selectivity over the constitutive proteasome (cPS) resulted in a larger therapeutic index in mouse models of various diseases [13-15]. In contrast, bortezomib and carfilzomib, FDA-approved drugs, primarily target chymotrypsin-like subunits (β5) in both cPS and iPS. They are covalent inhibitors binding to the Thr1 residue with the boronic acid warhead of bortezomib and with the epoxide warhead of carfilzomib. The β5 binding sites of iPS and cPS are highly similar; however, selectivity can be achieved primarily in the sequentially identical S1 pocket that is more spacious in iPS. Interestingly, covalent inhibitors with oxathiazolone warhead were found to exhibit inherent iPS selectivity that is modulated by oxathiazolone substituents [12,16,17].

Covalent inhibitor binding is a two-step process starting with the formation of a noncovalent complex where the electrophilic warhead of the ligand is placed in the proximity of the nucleophilic residue. The second step is the chemical reaction between nucleophilic sidechains equipped with nucleophilic groups, such as lysine (NH_2), cysteine (SH), serine (OH), threonine (OH) and the warhead of the ligand. The optimization of these steps and thus the affinity and selectivity tuning of covalent inhibitors can be efficiently supported by computational methods [18,19]. The free-energy change accompanying the noncovalent complex formation can be calculated with force-field-based methods, most notably with free energy perturbation (FEP) and thermodynamic integration (TI) [20]. The calculation of the energy change associated with covalent bond formation requires quantum mechanics to properly describe the electron rearrangement during the chemical reaction. Although high-level QM calculations are able to accurately describe chemical reactions of small- to medium-sized systems [21], they are unfeasible for large systems involved in biochemical reactions. An appealing alternative is the application of QM/MM mixed potentials in which the chemically interesting region of the system is treated by quantum mechanics, while the rest of the atoms are described by force-field parameters [22]. However, using high-level quantum theory in QM/MM molecular dynamics simulations is still computationally challenging, and the application of approximate schemes such as the semiempirical wavefunction or DFT methods is a good tradeoff between accuracy and resource requirements. We have shown that TI used for calculating the noncovalent affinity and semiempirical DFTB3 used for assessing reactivity can be combined to quantitatively account for covalent inhibitory activity and selectivity [19].

Noncovalent complex formation can be considered a fast equilibrium process that is characterized by the K_i equilibrium constant. The covalent reaction is typically associated with a higher barrier and is either reversible or irreversible depending on the mechanism and free-energy profile of the reaction. Irreversible covalent binding is characterized by the rate constant k_{inact} (Eq. (1)).

$$E + I \underset{\rightleftharpoons}{K_i} E \cdot I \xrightarrow{k_{inact}} E - I \ (E : enzyme; I : inhibitor) \tag{1}$$
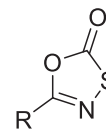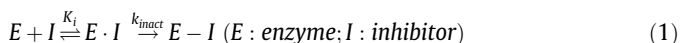

Fig. 1. General formula of 1,3,4-oxathiazol-2-ones.

Both steps may play an essential role in the ligands' overall binding affinity; therefore, both K_i and k_{inact} are needed for the complete description of the inhibition. K_i and k_{inact} can be determined experimentally and can be computed as outlined above. However, the experimental determination of the individual K_i and k_{inact} values may be difficult, and inhibitors are sometimes characterized by the k_{inact}/K_i ratio. We [19] and others [23-25] have shown that free energy changes and corresponding K_i and k_{inact} values and the k_{inact}/K_i ratio can be calculated with an accuracy useful in covalent inhibitor design.

The present work addresses a complete characterization of the mechanism and free energy profile of immunoproteasome inhibition by compounds with oxathiazolone warheads. A series of 1,3,4-oxathiazol-2-ones (Fig. 1) were found to inhibit the *Mycobacterium tuberculosis* (MTB) proteasome, and these compounds were proved to be selective against the human constitutive proteasome [16]. It was later shown for an extended set of oxathiazolones that they inhibit the human immunoproteasome β5i subunit and exhibit significant selectivity over the constitutive proteasome [17]. Psoralen derivatives with oxathiazolone warhead were also found to selectively inhibit iPS [12]. The observed inhibition profile of oxathiazolones renders these compounds attractive as therapeutic agents. Although their aqueous stability is limited, compounds with improved stability have also been reported [26]. The binding sites of the MTB proteasome and iPS contain a larger S1 pocket than does cPS [16,27,28], and this was proposed to contribute to the observed inhibition profile of oxathiazolones [17]. Remarkably, cyclocarbonylation of Thr1 by oxathiazolone resulted in an important shift of the loop near the active site in the MTB proteasome [16]. However, no data on the inhibitory mechanism and the activity and selectivity profile of oxathiazolones against iPS have been published.

Here, we aim to explore the detailed mechanism of the binding of oxathiazolone derivatives to the human immunoproteasome. The identified mechanism and the corresponding free energy profile allow us to find the rate-determining step and the corresponding rate constant that most influences k_{inact}. By performing calculations for K_i by thermodynamic integration and k_{inact} by QM/MM MD simulations using umbrella sampling, we characterized several oxathiazolone inhibitors and compared computational values to experimental k_{inact}/K_i ratios. Moreover, calculations for both cPS and iPS with compounds showing significant selectivity identify selectivity determinants—in particular, the contribution of noncovalent and covalent complex formation. The procedure validated by experimental results can be used to support the design of selective immunoproteasome inhibitors.

2. Materials and methods

2.1. System preparation and docking of HT1146

HT1146 was selected as a suitable compound for easy transformation with thermodynamic integration (see below). The starting structure was extracted from PDB 5M2B [11], the x-ray structure of 20S yeast proteasome with human β5i and β6i subunits complexed with thiazole based inhibitor **Ro19**. The β5i subunit was kept. The preparation was performed with Schrödinger's Maestro [29] module and consisted of filling the missing atoms and loops, deleting

waters, optimizing the hydrogen bond network and alleviating steric clashes with constrained minimization. The minimized structure was used for ligand docking to achieve starting structure for both the thermodynamic integration and QM/MM MD simulations. The grid for docking was generated by selecting the centre of mass of **Ro19** as the centre of the grid having 25x25x25 Å³ outer and 10x10x10 Å³ inner box volume. Once the grid was generated, ligand **HT1146** was docked into the β5i subunit and the ten best poses were saved. The most feasible structure of the **HT1146**-β5i complex was selected by visual inspection and was used for further examinations. Both grid generation and docking were performed with Glide [30-32].

2.2. Calculation of the non-covalent binding free energy differences using thermodynamic integration

Ligands complexed with the β5i subunit were generated by modifying the docked **HT1146** into the actual ligand structure, assuming the same binding mode for all the examined oxathiazolones. Construction of the MD system and thermodynamic integrations were carried out by the AMBERtools18 software package [33] following the dual-topology protocol. Both the ligands and the complexes were immersed into an octahedral TIP3P [34] water box using tLEaP. System neutralization was achieved by adding sodium or chloride ions depending on the overall charge of the constructed system. The solvent box preparation was followed by a multistep relaxation protocol, namely 1000 steps of steepest descent minimization, 50 ps of NVT heating to 310.15 K and 1 ns of NPT equilibration. The above steps were performed for the solvated ligand and complex systems including their recharge, decharge and vdw (see below) structure at the λ value of 0.5 (**Figures S1 and S2**). The alchemical transformation during the thermodynamic integration involved 3 steps: the removal of the softcore atoms' partial charge (decharge), modification of the neutral softcore atoms into the perturbed structure (Van der Waals, vdw step), and reintroduction of the partial charges into the perturbed atoms (recharge) (**Figure S1**). Each step used windows with evenly separated lambda coupling parameter values ranging from 0.0 to 1.0 with 0.1 increment. The windows were consisted of two substeps: a 20 ps long heating to 310.15 K and a 1 ns long thermodynamic integration in NVT ensemble. SHAKE [35] was enabled for the non TI region atoms, while NOSHAKE was applied for the softcore hydrogens. Every above-mentioned MD simulation was performed with 1 fs time step using the FF14SB [36] force field. The evaluation of the ΔΔG free energy differences from the resulted outputs was carried out with the analyse.sh [37] script available at AMBER's website. For temperature regulation, the Langevin thermostat was applied with the collision frequency of 2 ps⁻¹, while pressure was maintained by the Berendsen barostat with 2 ps relaxation time. Details of thermodynamic integration steps and their results are shown in **Figure S3** and **Table S1**.

The estimation of the binding free energy difference between **HT1146** and **HT2004** in cPS was performed similarly. Structure of the cPS was extracted from PDB 4R67. The covalently bound ligand was deleted and the neutral form of Thr1 was rebuilt. Binding poses of **HT1146** and **HT2004** in cPS were imported from the iPS enzyme-ligand complexes after structure alignment of iPS and cPS by Maestro's built-in tool. The following steps were identical to those described above for the thermodynamic integration in iPS.

2.3. Selectivity calculation by thermodynamic integration with sidechain mutation

Following our previously developed protocol [19] we estimated the binding free differences of selected ligands between iPS and cPS by thermodynamic integration using Gln53Ser sidechain muta-

tion. The structure of the "hybrid cPS" was prepared by mutating the Gln53 residue to Ser53 in the previously used non-covalent iPS structure. The thermodynamic integration followed a single topology model, in which the sidechain is modified directly in one step, both with and without the inhibitor molecules. The overlapping backbones of the original and mutant proteins were merged with ParmEd, both systems were immersed in an octahedral box of TIP3P waters and relaxed by the same protocol as described for iPS above. The 1 ns, NVT productive MDs were carried out after 20 ps NVT heating and equilibration for each λ window. λ was varied from 0.0 to 1.0 with 0.1 increment. The evaluation of the ΔΔG between the complex and apo forms were carried out as described above for iPS.

2.4. Error estimation in thermodynamic integration

The errors of the TI simulations were estimated by a transformation loop starting with **HT1146** and returning to it through a sequence of ligand modifications using TI simulations. The error is given as the sum of the ΔΔG values of the cycle's TI steps, as the theoretical value of the ΔΔG in such a cycle is 0 kcal/mol. Detailed results of the TI error estimation are shown in **Figures S4-S5** and **Table S2**.

2.5. Inhibitory mechanism of HT1146 by QM/MM MD simulations

The **HT1146**-enzyme complex obtained by docking (see above) was immersed into an octahedral water box of TIP3P waters. The constructed system was subject to the following relaxation protocol: 1000 steps of steepest descent minimization with constrained heavy atoms, 1000 steps of steepest descent minimization without constraint, 100 ps NVT heating to 310.15 K and 4 ns NPT equilibration at 310.15 K. All these steps were performed using FF14SB MM force field. QM/MM mixed potential was introduced in a following 100 ps NVT MD also at 310.15 K. The QM region was described with DFTB3 potential [38] and composed of the ligand, the Thr1 residue and the CαH-NH fragment of the Thr2 residue (**Figure S6**), while the rest of the atoms were treated by FF14SB force field. The link atom approach was used to separate the QM and MM subsystems. The relaxed structure was subjected to a series of 50 ps back and forth QM/MM steered molecular dynamic (SMD) simulations using the PLUMED [51] patch to control the bias potentials applied to the reaction coordinates during the simulations. The spring constant was set to 300 kcal/(mol·Å²). After forward–backward-forward SMD simulations, structures were extracted at 0.1 Å increments along the reaction coordinate (RC) from the second forward pulling and used as starting structures for the umbrella sampling (US) windows. Further information belonging to the SMDs, reaction coordinates and frame extractions are available in **Figures S7 and S8**. QM/MM MD US simulations were performed in NVT ensemble with 40 ps long simulation windows with 300 kcal/(mol·Å²) force constant. The increments between the center of the windows were 0.1 Å RC value, the overlap between windows was inspected by histogram analysis. The first 5 ps of every window was discarded as relaxation, while the output of the rest of the simulations was used to generate the potential of mean force (PMF). The weighted histogram analysis method [39] (WHAM) was used to construct the PMFs of the reaction steps. The number of bins was set to three times the number of windows, while the tolerance parameter was set to 0.0001. The force constant in the wham metafile was set to 300 kcal/(mol·Å²) as PLUMED - in contrast to AMBER – defines the force constant in the same way as WHAM [40]. Statistical uncertainties were estimated by the bootstrapping algorithm using ten fake data sets with correlation time set to 140 derived from the auto-correlation functions of previous simulations. The complete continuous free energy

profiles of the two examined reaction mechanisms were constructed by joining the consecutive reaction steps' PMFs; The PMFs of the subsequent steps were joined at their minima and this procedure was justified by the inspection of the structural continuity between the reaction steps.

2.6. PMF calculation of the rate-determining step for other compounds

Structure of the product state of the first step of the carbonate mechanism obtained with **HT1146** was extracted from the RC = 1.5 window's final frame. The solvent molecules were deleted, and the ligand was modified into the inhibitor structure to be examined. The new ligand-enzyme complex was treated with a shortened relaxation protocol, including 1000 steps of steepest descent minimization, 20 ps NVT heating to 310.15 K and 100 ps NPT equilibration at 310.15 K. The QM/MM approach was applied for all three steps. Interatomic distance constraints were applied to preserve the arrangement of the ligand inside the binding pocket. Back and forth, SMD simulations were performed for the rate-determining step in the same manner as it was described for **HT1146** above. (**Figure S9**) The final trajectory was used for frame extraction for umbrella sampling. The US simulation and the PMF construction was identical to what was already described for **HT1146** above.

PMF calculations of the rate determining step for **HT1146** and **HT2004** in cPS were performed similarly to those in iPS. The previously used non-covalent structure of cPS derived from PDB 4R67 was modified by deprotonating the Oγ and protonating the terminal amino group. The starting pose of ligand molecules were extracted from the iPS-ligand complexes after protein structure alignment. System preparation, relaxation, steered molecular dynamics and umbrella sampling were performed as described above for iPS.

2.7. QM corrections

QM correction for the DFTB3 potential was performed with the Gaussian 16 program package [41]. After the construction of the full PMF of the two reaction mechanisms, the reactant, intermediate, product and transition state (TS) structures were extracted as the last frame of the simulation window belonging to the RC of the minima or the TS. The non-QM atoms, and selected QM atoms were deleted keeping the size of the system at the minimum for the high-level QM calculations. The geometry of the extracted structures were optimized with B3LYP functional and 6-31G++(d,p) basis set using the implicit PCM solvent model. For stable structures, the OPT keyword was used to perform geometry optimization, while for transition states, the bond lengths forming the reaction coordinate were frozen using the OPT = modredundant keyword of Gaussian. This was followed by single point calculations at the DFTB3 and ωB97XD/aug-cc-PVTZ levels of theory in vacuum, as no PCM model is available for DFTB3 in Gaussian. The correction was calculated as the difference between the ωB97XD and DFTB3 energies.

3. Results and discussion

The covalent inhibition of the immunoproteasome by an extensive set of oxathiazolone compounds was experimentally characterized in ref. [17]. The inhibition constant K_i of noncovalent binding and the rate constant k_{inact} of covalent binding are presented for several compounds, while the k_{inact}/K_i ratios are reported for some less potent inhibitors. These data provide a sound basis to validate computational studies aiming at a detailed description of the mechanism of oxathiazolone binding to the immunoproteasome. The calculation of K_i characterizing the non-covalent binding is relatively straightforward by thermodynamic integration, although it should be noted that no experimental structure of the binding mode before the chemical reaction is available; rather, it must be predicted computationally. The calculation of the rate constant k_{inact} is more challenging since the mechanism of the chemical reaction is unknown. Here, the first step is to explore the reaction mechanism and to identify the rate-determining step, or steps, that most affect k_{inact}.

The experimental K_i and k_{inact} values are related to the binding free energy (ΔG_b) and to the reaction barrier ($\Delta G^{\ddagger}$), respectively, by Eqs (2) and (3).

$$\Delta G_b = RT \ln (K_i) \tag{2}$$

$$\Delta G^{\ddagger} = -RT \ln \left(\frac{k_{inact}}{k_b T/h} \right) \tag{3}$$

where R is the universal gas constant, T is the absolute temperature, k_b is the Boltzmann constant, and h is the Planck constant. Binding free energy differences and reaction barrier free energies can be calculated and converted into K_i and k_{inact} values using Eqs (2) and (3), respectively. In the forthcoming discussion, we first present our results concerning the covalent step—namely, the reaction mechanism exploration and k_{inact} calculations. This is followed by the results of the K_i determinations and the comparison of the experimental and computed quantities. The iPS versus cPS selectivity was also evaluated and compared for two ligands. Finally, we analyse the inhibitory mechanism and the role of the two consecutive steps in determining inhibitory activities and selectivities.

3.1. Exploration of the covalent reaction mechanism

Two mechanisms were proposed for covalent inhibition by compounds with oxathiazolone warheads [16]. Both mechanisms (Fig. 2) start with the activation of the hydroxyl group of Thr1 by abstracting its proton by the terminal amine group of the residue. The reaction pathway branches at the nucleophilic attack of negatively charged oxygen. Depending on which bond breaks during the reaction, C-S or C-O, we label the route as the carbonate or carbonthioate route, respectively. Both routes include proton transfer from the Thr1 terminal NH_3^+ group. It is followed by a second nucleophilic attack, in which the amine nitrogen attacks the electrophilic carbon, while the remaining bond between the ligand and the enzyme, C-O in the carbonate and C-S in the carbonthioate route, breaks. Proton transfer from the amine to the leaving group yields the same product structure for both pathways. After the oxazolidinone ring is formed, the residual compound decomposes into an amide while the sulfur atom leaves the molecule; however, this does not affect the binding events. It also has been proposed [16] that the hydrolysis of both INT2 and INT2′ can lead to the decomposition of oxathiazolone, while the enzyme preserves its activity. In the current study, we focus on the inhibition mechanisms shown in Fig. 2.

The reaction of the Thr1 residue of the proteasome with several ligands has been investigated, and varying protonation states of the active site residues have been proposed [42]. The nucleophilic attack of Thr1 Oγ is accompanied by proton transfer either to the Nε of Lys33 [43,44] or to the terminal amine of Thr1 [45,46]. The proton transfer between the OγH and NH_2 groups of Thr1 can proceed either directly or via a water molecule. The relative positions of the OγH and NH_2 groups are compatible with both direct and water-mediated proton transfer. Previous theoretical studies of the human proteasome suggest a ligand-dependent proton transfer mechanism; peptide hydrolysis starts with water-mediated proton transfer [47], while the first step in covalent inhibition by syringo-
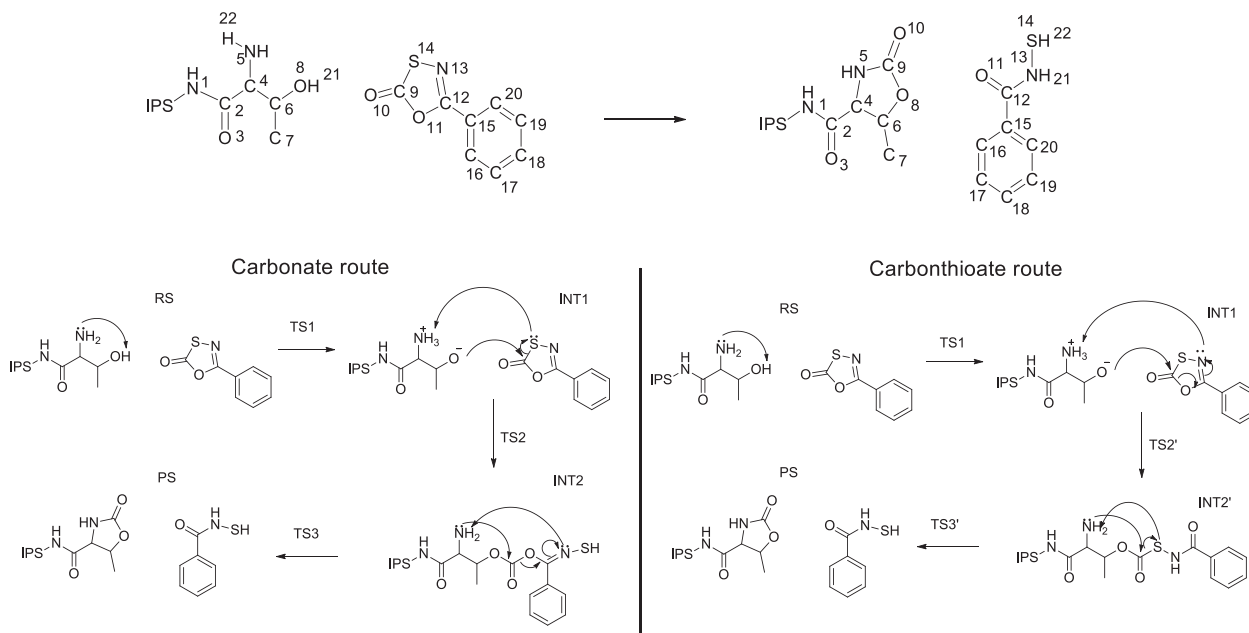
Fig. 2. Examined reaction mechanisms of **HT1146** with IPS. Atom numbering is shown in the overall reaction scheme on the top.

lin A [46] and epoxomicin [45] is direct proton transfer. The analysis of the 4 ns MD trajectory of the **HT1146**-IPS noncovalent complex showed that the proximity of a water molecule to the Thr1 residue is very rare, and we investigated only the direct proton transfer between the OγH and NH_2 groups of Thr1. This is in line with the proposed proton transfer in the presence of other covalent inhibitors [45,46]. We found that the DFTB3/FF14SB potential yields a stable activated Thr1 residue with deprotonated Oγ interacting with the protonated Thr1 NH_3^+ and Lys33 NH_3^+ groups. The free energy profile for this proton transfer yielding INT1 is shown in Fig. 3 and is similar to that obtained with B3LYP/6–31++G**: FF14SB potential [45,46].

3.1.1. Carbonate route

The formation of the second intermediate (INT2) includes O8-C9 bond formation and proton transfer from N5 to S14 (Fig. 2). SMD work curves for this step were generated with reaction coordinates created as various combinations of the relevant atom
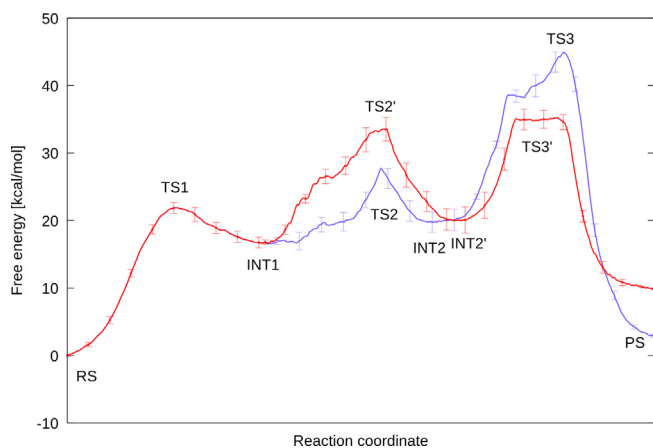

Fig. 3. Calculated PMF curves for the carbonate (blue) and carbonthioate (red) pathways of **HT1146**. Structure labels are identical to those in Fig. 2. Statistical errors are represented with error bars. (For interpretation of the references to colour in this figure legend, the reader is referred to the web version of this article.)

distances. Simulations yielded work curves corresponding to an asynchronously concerted process in which the formation of the O8-C9 bond is fairly advanced when the proton moves from N5 to S14. Equivalent results were obtained with umbrella sampling simulations using structures from two-dimensional SMD simulations along the (C9-S14)–(O8-C9) and (N5-H22)–(S14-H22) distance combinations (**Figure S10**). The next step, the transformation of INT2 into the product (PS), involves the attack of N5 on C9 and proton transfer from N5 to N13. We observed that N5-C9 bond formation and C9-O11 bond breaking are followed by a rotation along the C15-C12 bond that brings N5 and N13 into a relative position, facilitating proton transfer between them. The driving force of the rotation around the C15-C12 bond appears to be the interaction between the O11 carbonyl oxygen and the positively charged amine group of Lys33. This interaction stabilizes the transient formation of excess negative charge on the leaving group in the ring formation reaction.

3.1.2. Carbonthioate route

This mechanism differs from the carbonate route starting at the transformation of the first intermediate (INT1) to the second intermediate (INT2′). O8 of the activated threonine Thr1 attacks C9 similarly to the analogous step in the carbonate route, but INT2′ is formed by the breakage of the C9-O11 bond and by proton transfer from N5 to N13 (Fig. 2). Proton transfer asynchronously occurs in the same step with C-O bond formation, analogous to what was found in the carbonate route. The transformation of INT2′ into PS starts with N5 attack on C9, just as in the carbonate route; however, the proton transfer from N5 to the leaving group needs no conformational rearrangement, as the S14 atom is in a proper position to accept the proton. Nevertheless, N5-C9 bond formation is advanced with respect to N5-S14 proton transfer.

3.2. Reaction free energy profiles

Once full trajectories for both mechanisms were available by SMD simulations, we performed QM/MM MD umbrella sampling calculations. The potential of mean force (PMF) curves constructed with WHAM are shown in Fig. 3.

The formation of INT1 is identical in both pathways, as it is the common threonine activation step. This proton transfer from O8 to N5 has a significant barrier and is endothermic. The reaction between INT1 and INT2 corresponds to nucleophilic attack by deprotonated oxygen coupled with proton transfer from N5. The formation of the O8-C9 bond is accompanied by the breakage of the C9-S14 or the C9-O11 bond in the carbonate and carbonthioate routes, respectively. It is common in the two routes that proton transfer (either to N13 or to S14) follows bond formation, but no intermediate is formed in either case. For both routes, the barriers are slightly higher than that of the first proton transfer, and the second intermediates (INT2 and INT2′) have slightly higher free energy than INT1. The reaction between INT2 and PS includes nucleophilic attack by the amine group of the Thr1 residue and final proton transfer. In both routes, these steps are consecutive without a well-defined intermediate state, as no local free energy minimum is observed between INT2 and PS (Fig. 3). However, the carbonate route includes a conformational rearrangement required to bring the N13 atom into an appropriate position to accept a proton from N5.

The PMF curves of the carbonate and carbonthioate routes predict different reaction free energies, although the overall reaction free energy must be equal for the two routes. The reason for this reaction free energy difference is the structural differences at the product state; the alternative reaction routes and the different conformations of the products accompanied by varying enzyme-solvent environments explain the modest numerical difference in the reaction free energies. It must also be observed that the obtained reaction energies are positive for both routes. We also note that the experimental k_{inact} value of **HT1146** ($9.3 \cdot 10^{-4}$ s^{-1}) [17] corresponds to a barrier of 22.4 kcal·mol^{-1}, and this is largely overestimated by the calculations. These shortcomings of the computed free energies can be attributed to the inaccuracies of the approximate DFTB3 method. Several studies have shown [48-50] that QM/MM free energy calculations using DFTB3 for the QM region can be efficiently corrected to obtain free energy profiles in accordance with experimental data.

3.3. QM corrected free energy profiles

Free energies obtained for the reaction state, transition states, intermediate states and product states were included in the correction. PMF corrections were obtained as the difference between ωB97XD and DFTB3 single point energies calculated for the atoms directly participating in the chemical reactions (see the details in the Methods section). The results of the QM calculations and the corrected PMF are shown in Table 1 and in Fig. 4.

The correction by high-level QM calculations significantly change the free energy profile of the reactions. The corrected
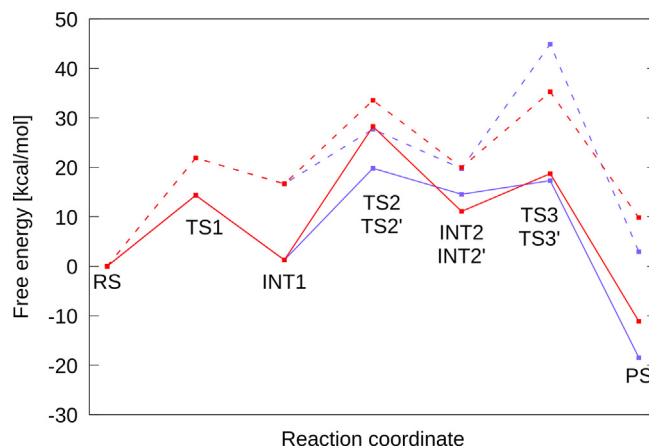
Fig. 4. Original (dashed line) and QM corrected (straight line) free energy profiles for the reaction of **HT1146** with IPS calculated on the carbonate (blue) and carbonthioate (red) pathways. (For interpretation of the references to colour in this figure legend, the reader is referred to the web version of this article.)

barrier and reaction energy levels suggest that the carbonate mechanism is favoured over the carbonthioate mechanism. Interestingly, the transition barrier of the third step in both cases is lowered so that the second step—namely, the nucleophilic attack of the activated Thr1 oxygen and the accompanying proton transfer—is the rate-determining step. The corrected barrier height for the carbonate route is 19.8 kcal·mol^{-1}. This value is lower than the 22.4 kcal·mol^{-1} obtained from the experimental k_{inact} value, but it indicates sensible reaction free energy profiles after QM correction.

3.4. Free energy barrier of the rate-determining step of other oxathiazolones

Further umbrella sampling calculations were carried out for oxathiazolone compounds (Fig. 5) to compute the k_{inact} values using Eq. (3). These compounds from ref. [17] were selected to maximize the range of inhibitory activity as expressed with the k_{inact}/K_i ratio. As the activation step of the Thr1 residue is considered to be ligand independent, only the barrier of the rate-determining step was calculated. This barrier was corrected by the QM correction derived for the same step for **HT1146** and was added to the reaction free energy of the first step. The resulting PMF curves are shown in **Figure S11**, and the corresponding $\Delta G^{\ddagger}$ values are presented in Table 2. The calculated $\Delta G^{\ddagger}$ values are higher for the less active compounds **HT1071** and **HT2210**, showing that the activity drop for these compounds is connected with

Table 1
Results of the QM correction calculations. All entries are energies in kcal·mol^{-1} units. The amount of correction is the difference between the ωB97XD and DFTB3 energies.

| Carbonate route							
Structure	RS	TS1	INT1	TS2	INT2	TS3	PS
wb97xd SP	0.0	27.1	45.7	12.0	3.6	9.3	−22.9
DFTB3 SP	0.0	34.7	61.1	19.9	8.8	36.9	−1.5
Difference	0.0	−7.5	−15.4	−7.9	−5.2	−27.6	−21.4
PMF	0.0	21.9	16.7	27.7	19.8	44.9	2.9
Corr. PMF	0.0	14.4	1.3	19.8	14.6	17.3	−18.5
Carbonthioate route							
Structure	RS	TS1	INT1	TS2′	INT2′	TS3′	PS
wb97xd SP	0.0	27.1	45.7	33.2	−9.1	−12.7	−21.4
DFTB3 SP	0.0	34.7	61.1	38.5	−0.2	3.8	−0.4
Difference	0.0	−7.5	−15.4	−5.3	−8.9	−16.5	−21.0
PMF	0.0	21.9	16.7	33.6	20.0	35.3	9.8
Corr. PMF	0.0	14.4	1.3	28.3	11.1	18.7	−11.1
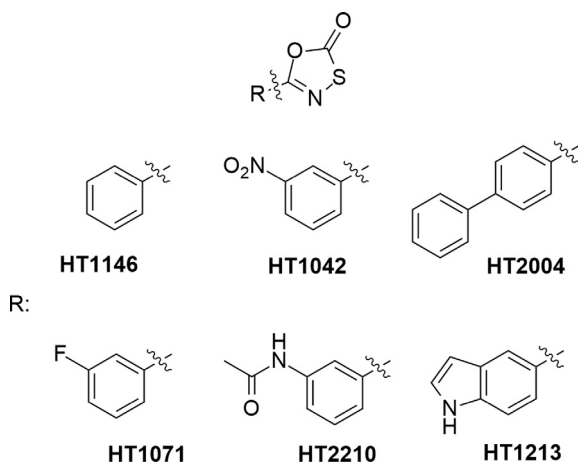
Fig. 5. Investigated IPS inhibitors.

lower k_{inact}—i.e., lower reactivity—and this is more pronounced for **HT2210.**

3.5. Binding free energies of the noncovalent complex

The calculation of the inhibitory activity and the complete free energy profile of the two-step binding mechanism of covalent inhibitors requires the evaluation of the binding free energy of the noncovalent binding preceding the covalent binding step, as shown by Eq. (1). To characterize the noncovalent step, classical MD coupled with thermodynamic integration was used. All examined inhibitors (Fig. 5) are equipped with an oxathiazolone warhead and inhibit the immunoproteasome by covalently binding to Thr1. The X-ray structure of the β5i subunit of the immunoproteasome complexed with **Ro19** (PDB: 5M2B) was used. Docking of **HT1146** into the protein was used to generate the enzyme-ligand complex. Note that only ligand **HT1146** was docked into the active site, as it was used as a reference molecule, and the starting positions of further compounds were constructed by modifying it inside the binding pocket. The scheme of the transformation steps and the complete description of the TI method can be found in the Methods section and in the SI.

The calculated binding free energies together with the experimental noncovalent binding energies are shown in Table 2. Binding free energy differences obtained by thermodynamic integration were converted into binding free energies by minimizing the root-mean-square deviation (RMSD) from the experimental results. This shift does not bias the correlation between the calculated and experimental data and does not affect the compound ranking. The calculated K_is together with the k_{inact} values were used to characterize the inhibitor binding as described below.

3.6. Selectivity between iPS and cPS

HT1146 exhibited slight selectivity with k_{inact}/K_i = 118 and 31.3 $M^{-1}s^{-1}$ for iPS and cPS, respectively, while **HT2004** was vastly more active against iPS, as shown by k_{inact}/K_I = 1093 and 0.23 $M^{-1}s^{-1}$ for iPS and cPS, respectively. To analyse the significant selectivity of **HT2004** and the difference in selectivities between **HT1146** and **HT2004**, we performed further calculations. We note that the differences in k_{inact}/K_i can be expressed with free energy differences in the following way:

$$\log\left(\frac{k_{inact}[A]}{K_i[A]}\right) - \log\left(\frac{k_{inact}[B]}{K_i[B]}\right)$$
$$= \frac{\log(e)}{RT}\left(-G^{\#}[B] + G^{\#}[A] - G_b[B] + G_b[A]\right)$$
$$= \frac{\log(e)}{RT}\left(-\Delta G^{\#} - \Delta G_b\right) \tag{4}$$

where $G^{\#}[A]$ and $G_b[A]$ are the activation free energy and the noncovalent binding free energy for compound A, respectively. The free energy difference obtained from the experimental data by Eq. (4) can be compared to the calculated free energy differences obtained with QM/MM umbrella sampling simulations for the barriers and with thermodynamic integration for the noncovalent binding free energy difference. Note that Eq. (4) refers to different compounds in the same protein; however, an analogous equation can be written for a compound that binds to two similar proteins. In this latter case, thermodynamic integration includes mutation of the protein, in our case mutation of iPS to cPS.

The barriers of the rate-determining step in iPS were formerly calculated, and they were complemented by barriers in cPS for both compounds using QM/MM umbrella sampling simulations. The difference in the noncovalent affinity of **HT1146** and **HT2004** towards iPS was formerly evaluated (Table 2). The **HT1146** to **HT2004** mutation was also performed in cPS. Experimentally derived and calculated free energies for the **HT1146** to **HT2004** mutation are shown in Table 3.

The transformation of iPS to cPS in water and in complex with a ligand provides us with a binding free energy difference of the ligand towards the two proteins. We selected the Gln53Ser mutation to transform the β5i iPS binding pocket into the β5c cPS binding pocket. Although these pockets have identical amino acid sequences, the different conformations of Met48 in β5i and β5c render the S1 pocket more spacious in β5i than in β5c [27,28]. The Met48 conformation was proposed to be affected by the Gln53Ser mutation; the interaction between Gln53 and Met48 in iPS is beneficial in an extended Met48 conformation that opens some space for the ligand between Ala49 and Met45.

Thermodynamic integration with the Gln53Ser mutation was performed in water and with the **HT1146** and **HT2004** complexes. The calculated binding free energy differences and previously calculated barrier free energies for covalent complex formation made

Table 2
Experimental inhibition constants for the noncovalent binding (K_i), corresponding binding free energies (ΔG_b), experimental inhibition rate constants for the covalent reaction (k_{inact}), corresponding free energy barriers ($\Delta G^{\ddagger}$) and experimental $\log(k_{inact}/K_i)$ values. Calculated binding free energies ($\Delta G_{b,calc}$), calculated free energy barriers ($\Delta G^{\ddagger}_{calc}$) and calculated $\log(k_{inact}/K_i)_{calc}$ values for the selected immunoproteasome inhibitors.

Compound	K_i [μM]	ΔG_b [kcal/mol]	k_{inact} x 10^3 [s^{-1}]	$\Delta G^{\ddagger}$ [kcal/mol]	$\log\left(\frac{k_{inact}}{K_i}\right)$[a]	$\Delta G_{b,calc}$ [kcal/mol]	$\Delta G^{\ddagger}_{calc}$ [kcal/mol]	$\log\left(\frac{k_{inact}}{K_i}\right)_{calc}$[a]
HT1146	7.90	-7.2	0.93	22.4	2.1	-7.3	19.8	4.0
HT2004	1.4	-8.3	1.54	22.1	3.0	-9.3	19.0	6.0
HT1042	0.42	-9.0	0.38	23.0	3.0	-8.2	21.7	3.2
HT1213	1.1	-8.5	0.26	23.2	2.4	-8.3	21.6	3.4
HT1071					1.3	-6.8	22.5	1.7
HT2210					1.9	-7.8	24.1	1.3

[a] k_{inact} is in s^{-1}, and K_i is in M units

Table 3

Comparison of experimental and calculated free energy differences between HT1146 and HT2004 binding (top two rows) and between binding to iPS and cPS (bottom two rows).

Transformation	Experimental[a] $-\Delta G^{\#}-\Delta G_b$ [kcal/mol]	Calculated[b] $\Delta G_{b,calc}$ [$-\Delta G^{\#}-\Delta G_b$] [kcal/mol]
HT1146->HT2004 iPS	−1.4	−2.0 [0.0[c]-2.0]
HT1146->HT2004 cPS	3.0	4.5 [5.0[d]-0.5]
HT1146 iPS->cPS	0.8	0.4 [2.0[e]-1.6]
HT2004 iPS-> cPS	5.1	6.7 [7.0[f]-0.3]

[a] The sum of $-\Delta G^{\#}-\Delta G_b$ is obtained from the experimental log(k_{inact}/K_i) difference using Eq.(4)

[b] The barrier ($\Delta G^{\#}$) for the rate-determining step and binding free energy differences (ΔG_b) are separately calculated. The sum and its components are shown as the difference between the barriers of **HT2004** (11 kcal/mol) and **HT1146** (11 kcal/mol) in iPS.

[d] Obtained as the difference between the barrier of **HT2004** (18 kcal/mol) and **HT1146** (13 kcal/mol) in cPS.

[e] Obtained as the difference between the barrier of **HT1146** in cPS (13 kcal/mol) and iPS (11 kcal/mol).

[f] Obtained as the difference between the barrier of **HT2004** in cPS (18 kcal/mol) and iPS (11 kcal/mol).

it possible to compare experimentally derived and computed free energies related to the inhibition of iPS and cPS by **HT1146** and **HT2004** (Table 3).

3.7. Evaluation of the overall proteasome inhibition

The experimental K_i and k_{inact} values when converted to binding free energies (ΔG_b) and reaction barrier free energies ($\Delta G^{\ddagger}$) cover narrow ranges of 2 kcal·mol^{-1} and 1 kcal·mol^{-1}, respectively. The free energies corresponding to the log(k_{inact}/K_i) values—namely, $-\Delta G_{bind}^{exp} - \Delta G^{\ddagger exp}$—also cover a narrow range of slightly over 1 kcal·mol^{-1} (top 4 entries in Table 2). This range is somewhat broader when less active compounds (**HT1071** and **HT2210**) are also considered. Therefore, we also calculated the K_i and k_{inact} values for these compounds, and log(k_{inact}/K_i)-s were compared to the experimental values (Table 2 and Fig. 6). (No individual K_i and k_{inact} were experimentally determined for these latter compounds.) The calculated and experimental log(k_{inact}/K_i) ratios show a reasonable correlation with $R^2 = 0.555$ (p(R) = 0.089) for the six investigated oxathiazolones. It was also observed that experimental log(k_{inact}/K_i) is correlated with calculated log($1/K_i$); the high coefficient of determination ($R^2 = 0.770$, p(R) = 0.022, **Figure S12**) is notable and shows that the differences in the noncovalent binding primarily affect the variation of the iPS inhibitory activity for these compounds. They have an identical warhead, and there is virtually no

electronic crosstalk with the noncovalent parts. Therefore, they should show similar reactivity that suggests the influence of noncovalent recognition. Indeed, the low calculated affinity for noncovalent complex formation by **HT1071** explains the low inhibitory activity, which is actually the lowest among the compounds investigated. However, the modest activity of **HT2210** is a result of limited noncovalent binding affinity and, more importantly, the low reactivity of this compound in the binding site of iPS. This observation indicates the potential effect of the binding mode on the reactivity, and its manifestation is discussed below in connection with iPS versus cPS selectivity.

The noncovalent complex of oxathiazolones places the carbonyl group in a position close to the OγH group of Thr1 and orients the substituent of the oxathiazolone ring towards the S1 binding pocket. This binding pocket is larger in the immunoproteasome [27] than in the constitutive proteasome, and we investigated how this structural difference together with our computational results can explain the observed similar inhibitory activity of **HT1146** towards iPS and cPS and the significant activity difference of **HT2004** towards these proteins. First, it is worth mentioning that the calculated free energy changes reasonably agree with the experimental free energy changes derived from activities (Table 3). The comparison is made for the cumulative process of noncovalent and covalent binding, as experimental data for the separate binding processes are not available for cPS. However, the good agreement between the experimental and calculated values makes confidence in the analysis of the computed components, ΔG_b, the binding free energy difference of the noncovalent binding and $\Delta G^{\#}$, the free energy barrier of the covalent bond formation. Computational results show that **HT2004** selectivity is primarily governed by different $\Delta G^{\#}$s in iPS and cPS. While noncovalent complex formation proceeds with minimal binding free energy alteration in iPS and cPS (-0.3 kcal/mol), the computed barrier is 7 kcal/mol higher in cPS than in iPS. An analysis of the transition state structures (Fig. 7) shows that **HT2004** binds to iPS with the proximal phenyl ring partially penetrating the extended space available in iPS. This extra space between Met45 and Ala49 is due to the extended conformation of Met45 and leads to a position of the oxathiazolone ring highly similar to that of **HT1146**. In contrast, Ser53 in cPS (Gln53 in iPS) forms an H-bond with the backbone carbonyl of Ala49 and does not allow Met45 to adopt the extended conformation and to open the space between Met45 and Ala49. Therefore, the proximal phenyl ring of the **HT2004**-cPS complex has a position shifted with respect to that in the **HT2004**-iPS complex and resembles that seen in the **HT1146**-cPS complex. However, **HT2004** is slightly rotated around the proximal phenyl ring to avoid steric clash between the terminal benzene ring and Val31. This rotation moves the oxathiazolone into a position different from its positions seen in the **HT1146**-iPS, **HT1146**-cPS and **HT2004**-iPS complexes. As a result of this shift of oxathiazolone, proton transfer to sulfur is hindered in the rate-determining step. The sulfur is shifted further from the attacking H atom; moreover, the interactions of the negatively charged sulfur atom with Thr21 amide and alcoholic hydrogens hamper it from approaching the proton donating nitrogen (Fig. 8). (Further representative structures of the stationary points of the reaction free energy curves are shown in **Figures S13-S15**.)

Our results show that the altered binding mode of **HT2004** in cPS has little effect on the noncovalent affinity, but it strongly affects the covalent reaction barrier. Remarkably, compounds with similar intrinsic reactivities may exhibit highly different reactivities in the protein binding pocket owing to small binding mode variations. The resulting changes in the position and interactions of atoms can significantly affect reactivity. This phenomenon has important implications for the affinity and selectivity of designed covalent inhibitors.
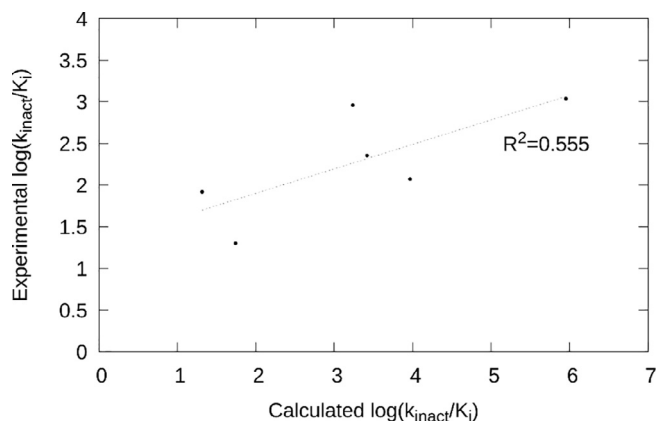
Fig. 6. Comparison of calculated and experimental log(k_{inact}/K_i) (k_{inact} in s^{-1} and K_i in M units).
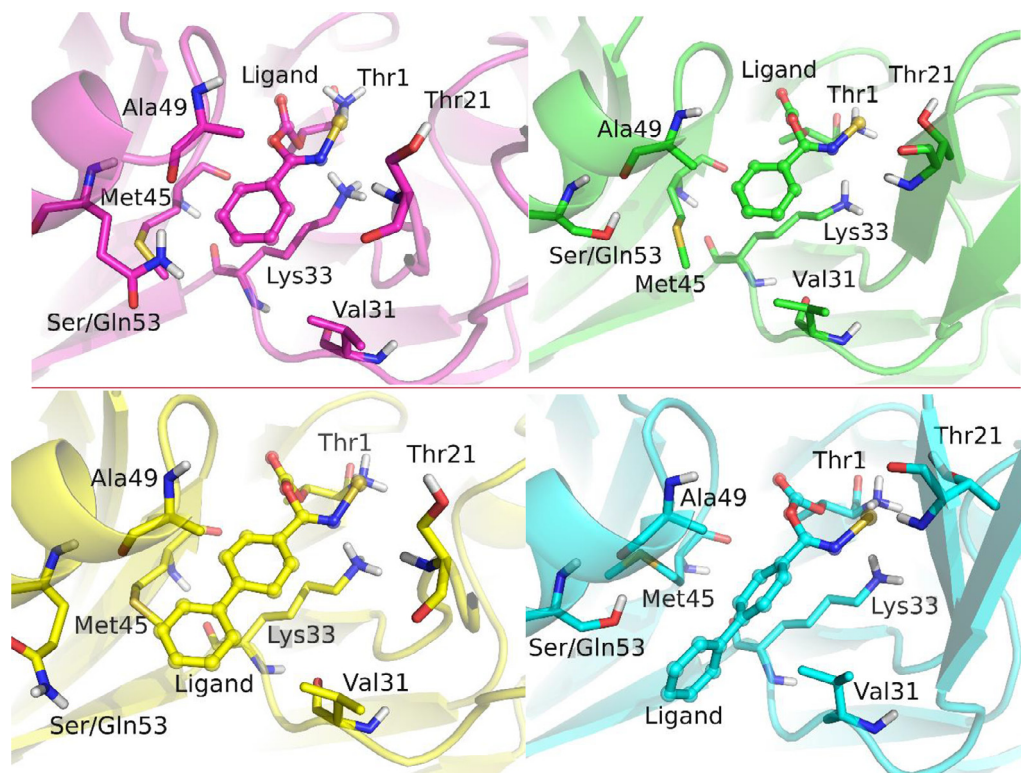
Fig. 7. Representative structures from umbrella sampling simulations around the transition states of the rate-determining step: **HT1146**-iPS (top left); **HT1146**-cPS (top right); **HT2004**-iPS (bottom left); **HT2004**-cPS (bottom right). The position of the oxathiazolone ring of **HT2004** in cPS is shifted owing to the lack of space between Met45 and Ala49 and to avoid steric clash with Val31.

4. Conclusions

The reaction mechanism leading to the irreversible inhibition of the immunoproteasome by compounds with oxathiazolone warheads was explored. Two formerly proposed mechanisms were investigated. Both start with the activation of the Thr1 residue by proton transfer between O8 (Oγ) and N5, the terminal NH_2 group of Thr1, and produce an intermediate (INT1) stabilized by neighbouring residues, most notably protonated Lys33. The second step starts with the nucleophilic attack of O8 on C9, the carbonyl carbon of the oxathiazolone ring. The carbonate route that includes the C9-S14 bond breaking after this nucleophilic attack exhibits a lower barrier and is more likely than the carbonthioate route where the C9-O11 bond breaks. O8-C9 bond formation in the carbonate route is followed by proton transfer between N5 and S14, resulting in the second intermediate (INT2). The reaction completes with oxazolidinone ring formation and detachment of the leaving group, leading to irreversible covalent inhibition of the target. DFTB3/FF14SB calculations with ωB97XD correction yield a free energy profile for the reaction with the formation of the second intermediate (INT2) as the rate-determining step.

The rate-determining step of covalent bond formation was simulated for five other oxathiazolone derivatives to obtain calculated barriers and corresponding k_{inact} values. The binding free energy of the noncovalent complex formation was also evaluated for the same compounds using classical forcefield-based thermodynamic integration. Binding free energies were converted into K_i equilibrium constants and calculated, and experimental K_i and k_{inact} values were analysed. The inhibitory activities of the compounds were characterized by $\log(k_{inact}/K_i)$, and a reasonable correlation ($R^2 = 0.555$) between the experimental and calculated values was

found. It was also observed that inhibitory activity variation is more affected by differences in the noncovalent affinity than in the reactivity. No individual K_i and k_{inact} were measured for less active compounds; however, computed K_i and k_{inact} values allow the contributions of the noncovalent and covalent complex formations to the inhibitory activity to be estimated.

The experimentally observed selectivity of oxathiazolone-based inhibitors for the immunoproteasome versus the constitutive proteasome can be rationalized by the binding mode and mechanism of these compounds. Their favourable binding mode places the oxathiazolone warhead in a position that facilitates nucleophilic attack by Thr1 Oγ and extends the substituent on the oxathiazolone ring towards the S1 binding pocket. This pocket is larger for the immunoproteasome than for the constitutive proteasome. The smaller **HT1146** compound fits similarly into the binding pocket of iPS and cPS and shows similar inhibitory potency for the two enzymes. In contrast, the more extended **HT2004** molecule adopts a moderately different binding mode in iPS versus cPS, which leads to a small difference in the noncovalent affinity but significantly affects the covalent reactivity. Thus, the two compounds with equivalent intrinsic reactivities show striking selectivity differences, which is attributed to the effect of the binding mode variation on the reactivity with the activated Thr1.

In summary, a plausible reaction mechanism for the covalent inhibition of the immunoproteasome by oxathiazolone derivatives was proposed. The identification of the rate-determining step allowed the calculation of the reaction barrier for several compounds. The binding free energy of the noncovalent binding was also evaluated. The complete energetic characterization of the binding made it possible to analyse the contribution of the noncovalent and covalent binding steps for compounds without experi-
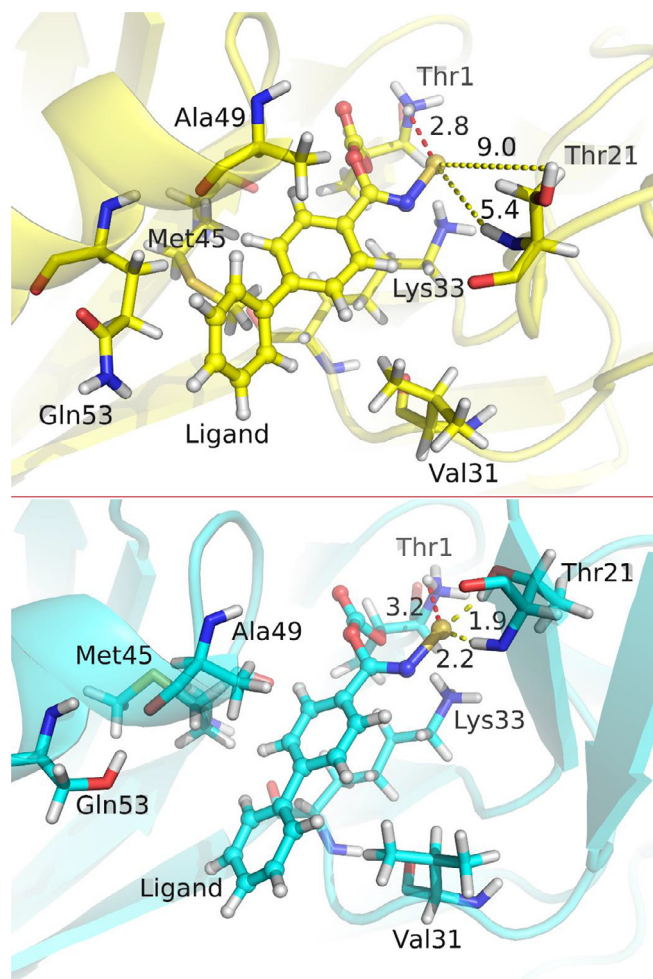
Fig. 8. **HT2004**-iPS (top) and **HT2004**-cPS (bottom) complex structures between the nucleophilic attack and the proton transfer of the rate-determining step. Distances between the ligand's sulfur atom and Thr21 Hγ and H are shown with yellow dashed lines. The distance between the transferred proton and the sulfur atom is shown with a red dashed line. (For interpretation of the references to colour in this figure legend, the reader is referred to the web version of this article.)

mentally determined individual K_i and k_{inact} values. The iPS versus cPS selectivity was attributed to reactivity differences caused by modest binding mode variation within the active sites.

CRediT authorship contribution statement

Levente M. Mihalovits: Investigation, Methodology, Writing - original draft. **György G. Ferenczy:** Methodology, Writing - original draft. **György M. Keserű:** Supervision, Writing - review & editing.

Declaration of Competing Interest

The authors declare that they have no known competing financial interests or personal relationships that could have appeared to influence the work reported in this paper.

Acknowledgements

Appendix A. Supplementary data

Supplementary data to this article can be found online at https://doi.org/10.1016/j.csbj.2021.08.008.

References

[1] Borissenko L, Groll M. 20S Proteasome and Its Inhibitors: Crystallographic Knowledge for Drug Development. Chem Rev 2007;107:687–717. https://doi.org/10.1021/cr0502504.
[2] Bedford L, Lowe J, Dick LR, Mayer RJ, Brownell JE. Ubiquitin-like protein conjugation and the ubiquitiny-proteasome system as drug targets. Nat Rev Drug Discov 2011;10:29–46. https://doi.org/10.1038/nrd3321.
[3] Nalepa G, Rolfe M, Harper JW. Drug discovery in the ubiquitin–proteasome system. Nat Rev Drug Discov 2006;5:596–613. https://doi.org/10.1038/nrd2056.
[4] Richardson PG, Sonneveld P, Schuster MW, Irwin D, Stadtmauer EA, Facon T, et al. Bortezomib or High-Dose Dexamethasone for Relapsed Multiple Myeloma. N Engl J Med 2005;352:2487–98. https://doi.org/10.1056/NEJMoa043445.
[5] Huber EM, Groll M. Inhibitors for the immuno- and constitutive proteasome: Current and future trends in drug development. Angew Chemie - Int Ed 2012;51:8708–20. https://doi.org/10.1002/anie.201201616.
[6] Baumeister W, Walz J, Zühl F, Seemüller E. The Proteasome: Paradigm of a Self-Compartmentalizing Protease. Cell 1998;92:367–80. https://doi.org/10.1016/S0092-8674(00)80929-0.
[7] Unno M, Mizushima T, Morimoto Y, Tomisugi Y, Tanaka K, Yasuoka N, et al. The Structure of the Mammalian 20S Proteasome at 2.75 Å Resolution. Structure 2002;10:609–18. https://doi.org/10.1016/S0969-2126(02)00748-7.
[8] Groettrup M, Kraft R, Kostka S, Standera S, Stohwasser R, Kloetzel P-M. A third interferon-γ-induced subunit exchange in the 20S proteasome. Eur J Immunol 1996;26:863–9. https://doi.org/10.1002/eji.1830260421.
[9] Griffin TA, Nandi D, Cruz M, Fehling HJ, Van Kaer L, Monaco JJ, et al. Immunoproteasome assembly: Cooperative incorporation of interferon γ (IFN-γ)-inducible subunits. J Exp Med 1998;187:97–104. https://doi.org/10.1084/jem.187.1.97.
[10] Kloetzel P-M, Ossendorp F. Proteasome and peptidase function in MHC-class-I-mediated antigen presentation. Curr Opin Immunol 2004;16:76–81. https://doi.org/10.1016/j.coi.2003.11.004.
[11] Cui H, Baur R, Le Chapelain C, Dubiella C, Heinemeyer W, Huber EM, et al. Structural Elucidation of a Nonpeptidic Inhibitor Specific for the Human Immunoproteasome. ChemBioChem 2017;18:523–6. https://doi.org/10.1002/cbic.201700021.
[12] Sosič I, Gobec M, Brus B, Knez D, Živec M, Konc J, et al. Nonpeptidic Selective Inhibitors of the Chymotrypsin-Like (β5 i) Subunit of the Immunoproteasome. Angew Chemie - Int Ed 2016;55:5745–8. https://doi.org/10.1002/anie.201600190.
[13] Kalim KW, Basler M, Kirk CJ, Groettrup M. Immunoproteasome Subunit LMP7 Deficiency and Inhibition Suppresses Th1 and Th17 but Enhances Regulatory T Cell Differentiation. J Immunol 2012;189:4182–93. https://doi.org/10.4049/jimmunol.1201183.
[14] Ichikawa HT, Conley T, Muchamuel T, Jiang J, Lee S, Owen T, et al. Beneficial effect of novel proteasome inhibitors in murine lupus via dual inhibition of type I interferon and autoantibody-secreting cells. Arthritis Rheum 2012;64:493–503. https://doi.org/10.1002/art.33333.
[15] Muchamuel T, Basler M, Aujay MA, Suzuki E, Kalim KW, Lauer C, et al. A selective inhibitor of the immunoproteasome subunit LMP7 blocks cytokine production and attenuates progression of experimental arthritis. Nat Med 2009;15:781–7. https://doi.org/10.1038/nm.1978.
[16] Lin G, Li D, De Carvalho LPS, Deng H, Tao H, Vogt G, et al. Inhibitors selective for mycobacterial versus human proteasomes. Nature 2009;461:621–6. https://doi.org/10.1038/nature08357.
[17] Fan H, Angelo NG, Warren JD, Nathan CF, Lin G. Oxathiazolones selectively inhibit the human immunoproteasome over the constitutive proteasome. ACS Med Chem Lett 2014;5:405–10. https://doi.org/10.1021/ml400531d.
[18] Lonsdale R, Burgess J, Colclough N, Davies NL, Lenz EM, Orton AL, et al. Expanding the Armory: Predicting and Tuning Covalent Warhead Reactivity. J Chem Inf Model 2017;57:3124–37. https://doi.org/10.1021/acs.jcim.7b00553.
[19] Mihalovits LM, Ferenczy GG, Keserű GM. Affinity and Selectivity Assessment of Covalent Inhibitors by Free Energy Calculations. J Chem Inf Model 2020;60:6579–94. https://doi.org/10.1021/acs.jcim.0c00834.
[20] De Vivo M, Masetti M, Bottegoni G, Cavalli A. Role of Molecular Dynamics and Related Methods in Drug Discovery. J Med Chem 2016;59:4035–61. https://doi.org/10.1021/acs.jmedchem.5b01684.
[21] Sirirak J, Lawan N, Van der Kamp MW, Harvey JN, Mulholland AJ. Benchmarking quantum mechanical methods for calculating reaction energies of reactions catalyzed by enzymes. PeerJ Phys Chem 2020;2:. https://doi.org/10.7717/peerj-pchem.8e8.
[22] Senn HM, Thiel W. QM/MM Methods for Biomolecular Systems. Angew Chemie Int Ed 2009;48:1198–229. https://doi.org/10.1002/anie.200802019.
[23] Yu HS, Gao C, Lupyan D, Wu Y, Kimura T, Wu C, et al. Toward Atomistic Modeling of Irreversible Covalent Inhibitor Binding Kinetics. J Chem Inf Model 2019;59:3955–67. https://doi.org/10.1021/acs.jcim.9b00268.

[24] Awoonor-Williams E, Abu-Saleh A-A-A-A. Covalent and non-covalent binding free energy calculations for peptidomimetic inhibitors of SARS-CoV-2 main protease. Phys Chem Chem Phys 2021(). https://doi.org/10.1039/d1cp00266j.

[25] Awoonor-Williams E, Rowley CN. Calculating the Full Free Energy Profile for Covalent Modification of a Druggable Cysteine in Bruton's Tyrosine Kinase. ChemRxiv 2020;1:1–11. 10.26434/chemrxiv.13132814.v1.

[26] Gryder BE, Guerrant W, Chen CH, Oyelere AK. Oxathiazole-2-one derivative of bortezomib: Synthesis, stability and proteasome inhibition activity. Medchemcomm 2011;2:1083. https://doi.org/10.1039/c1md00208b.

[27] Huber EM, Basler M, Schwab R, Heinemeyer W, Kirk CJ, Groettrup M, et al. Immuno- and constitutive proteasome crystal structures reveal differences in substrate and inhibitor specificity. Cell 2012;148:727–38. https://doi.org/10.1016/j.cell.2011.12.030.

[28] Hsu H-C, Singh PK, Fan H, Wang R, Sukenick G, Nathan C, et al. Structural Basis for the Species-Selective Binding of N, C-Capped Dipeptides to the Mycobacterium tuberculosis Proteasome. Biochemistry 2017;56:324–33. https://doi.org/10.1021/acs.biochem.6b01107.

[29] Schrödinger Release 2021-1: Maestro, Schrödinger, LLC, New York, NY, 2021.

[30] Friesner RA, Murphy RB, Repasky MP, Frye LL, Greenwood JR, Halgren TA, et al. Extra Precision Glide: Docking and Scoring Incorporating a Model of Hydrophobic Enclosure for Protein–Ligand Complexes. J Med Chem 2006;49:6177–96. https://doi.org/10.1021/jm051256o.

[31] Friesner RA, Banks JL, Murphy RB, Halgren TA, Klicic JJ, Mainz DT, et al. Glide: A New Approach for Rapid, Accurate Docking and Scoring. 1. Method and Assessment of Docking Accuracy. J Med Chem 2004;47:1739–49. https://doi.org/10.1021/jm0306430.

[32] Halgren TA, Murphy RB, Friesner RA, Beard HS, Frye LL, Pollard WT, et al. Glide: A New Approach for Rapid, Accurate Docking and Scoring. 2. Enrichment Factors in Database Screening. J Med Chem 2004;47:1750–9. https://doi.org/10.1021/jm030644s.

[33] Case DA, Ben-Shalom IY, Brozell SR, Cerutti DS, T.E. Cheatham I, Cruzeiro VWD, et al. AMBER 2018, University of California, San Francisco 2018.

[34] Jorgensen WL, Chandrasekhar J, Madura JD, Impey RW, Klein ML, Chandrasekhar JM, et al. Comparison of simple potential functions for simulating liquid water. J Chem Phys 1983;79:926–35. https://doi.org/10.1063/1.445869.

[35] Ryckaert JP, Ciccotti G, Berendsen HJC. Numerical integration of the cartesian equations of motion of a system with constraints: molecular dynamics of n-alkanes. J Comput Phys 1977;23:327–41. https://doi.org/10.1016/0021-9991(77)90098-5.

[36] Maier JA, Martinez C, Kasavajhala K, Wickstrom L, Hauser KE, Simmerling C. ff14SB: Improving the Accuracy of Protein Side Chain and Backbone Parameters from ff99SB. J Chem Theory Comput 2015;11:3696–713. https://doi.org/10.1021/acs.jctc.5b00255.

[37] Steinbrecher T, Loeffer HH. Small molecule binding to T4-lysozyme L99A http://ambermd.org/tutorials/advanced/tutorial9/ (accessed June 5, 2020).

[38] Yang Y, Yu H, York D, Cui Q, Elstner M. Extension of the self-consistent-charge density-functional tight-binding method: Third-order expansion of the density functional theory total energy and introduction of a modified effective coulomb interaction. J Phys Chem A 2007;111:10861–73. https://doi.org/10.1021/jp074167r.

[39] Kumar S, Rosenberg JM, Bouzida D, Swendsen RH, Kollman PA. THE weighted histogram analysis method for free-energy calculations on biomolecules. I. The method. J Comput Chem 1992;13:1011–21. https://doi.org/10.1002/jcc.540130812.

[40] Grossfield A. WHAM: an implementation of the weighted histogram analysis method

[41] Frisch MJ, Trucks GW, Schlegel HB, Scuseria GE, Robb MA, Cheeseman JR, et al. Gaussian 16, Revision A.03, Gaussian, Inc., Wallingford CT, 2016.

[42] Uranga J, Hasecke L, Proppe J, Fingerhut J, Mata RA. Theoretical Studies of the Acid-Base Equilibria in a Model Active Site of the Human 20S Proteasome. J Chem Inf Model 2021. https://doi.org/10.1021/acs.jcim.0c01459.

[43] Serrano-Aparicio N, Świderek K, Moliner V. Theoretical study of the inhibition mechanism of human 20S proteasome by dihydroeponemycin. Eur J Med Chem 2019;164:399–407. https://doi.org/10.1016/j.ejmech.2018.12.062.

[44] Serrano-Aparicio N, Moliner V, Świderek K. Nature of Irreversible Inhibition of Human 20S Proteasome by Salinosporamide A. The Critical Role of Lys-Asp Dyad Revealed from Electrostatic Effects Analysis. ACS Catal 2021;11:3575–89. https://doi.org/10.1021/acscatal.0c05313.

[45] Wei D, Lei B, Tang M, Zhan CG. Fundamental reaction pathway and free energy profile for inhibition of proteasome by epoxomicin. J Am Chem Soc 2012;134:10436–50. https://doi.org/10.1021/ja3006463.

[46] Wei D, Tang M, Zhan CG. Fundamental reaction pathway and free energy profile of proteasome inhibition by syringolin A (SylA). Org Biomol Chem 2015;13:6857–65. https://doi.org/10.1039/c5ob00737b.

[47] Wei D, Fang L, Tang M, Zhan CG. Fundamental reaction pathway for peptide metabolism by proteasome: Insights from first-principles quantum mechanical/molecular mechanical free energy calculations. J Phys Chem B 2013;117:13418–34. https://doi.org/10.1021/jp405337v.

[48] Ahsan M, Senapati S. Water Plays a Cocatalytic Role in Epoxide Ring Opening Reaction in Aspartate Proteases: A QM/MM Study. J Phys Chem B 2019;123:7955–64. https://doi.org/10.1021/acs.jpcb.9b04575.

[49] Lence E, van der Kamp MW, González-Bello C, Mulholland AJ. QM/MM simulations identify the determinants of catalytic activity differences between type II dehydroquinase enzymes. Org Biomol Chem 2018;16:4443–55. https://doi.org/10.1039/C8OB00066B.

[50] Mihalovits LM, Ferenczy GG, Keserű GM. Catalytic Mechanism and Covalent Inhibition of UDP- N -Acetylglucosamine Enolpyruvyl Transferase (MurA): Implications to the Design of Novel Antibacterials. J Chem Inf Model 2019;59:5161–73. https://doi.org/10.1021/acs.jcim.9b00691.

[51] Bonomi Massimiliano, Branduardi Davide, Bussi Giovanni, Camilloni Carlo, Provasi Davide, Raiteri Paolo, et al. PLUMED: A portable plugin for free-energy calculations with molecular dynamics. Computer Physics Communications 2009;180(10):1961–72. https://doi.org/10.1016/j.cpc.2009.05.011.